LETTERS

Polymorphism control of superconductivity and magnetism in Cs_3C_{60} close to the Mott transition

Alexey Y. Ganin[1]*, Yasuhiro Takabayashi[2]*, Peter Jeglič[3], Denis Arčon[3,4], Anton Potočnik[3], Peter J. Baker[5], Yasuo Ohishi[6], Martin T. McDonald[2], Manolis D. Tzirakis[2], Alec McLennan[1], George R. Darling[1], Masaki Takata[6,7], Matthew J. Rosseinsky[1] & Kosmas Prassides[2]

The crystal structure of a solid controls the interactions between the electronically active units and thus its electronic properties. In the high-temperature superconducting copper oxides, only one spatial arrangement of the electronically active Cu^{2+} units—a two-dimensional square lattice—is available to study the competition between the cooperative electronic states of magnetic order and superconductivity[1]. Crystals of the spherical molecular C_{60}^{3-} anion support both superconductivity and magnetism but can consist of fundamentally distinct three-dimensional arrangements of the anions. Superconductivity in the A_3C_{60} (A = alkali metal) fullerides has been exclusively associated with face-centred cubic (f.c.c.) packing of C_{60}^{3-} (refs 2, 3), but recently the most expanded (and thus having the highest superconducting transition temperature, T_c; ref. 4) composition Cs_3C_{60} has been isolated as a body-centred cubic (b.c.c.) packing, which supports both superconductivity and magnetic order[5,6]. Here we isolate the f.c.c. polymorph of Cs_3C_{60} to show how the spatial arrangement of the electronically active units controls the competing superconducting and magnetic electronic ground states. Unlike all the other f.c.c. A_3C_{60} fullerides, f.c.c. Cs_3C_{60} is not a superconductor but a magnetic insulator at ambient pressure, and becomes superconducting under pressure. The magnetic ordering occurs at an order of magnitude lower temperature in the geometrically frustrated f.c.c. polymorph (Néel temperature $T_N = 2.2$ K) than in the b.c.c.-based packing ($T_N = 46$ K). The different lattice packings of C_{60}^{3-} change T_c from 38 K in b.c.c. Cs_3C_{60} to 35 K in f.c.c. Cs_3C_{60} (the highest found in the f.c.c. A_3C_{60} family). The existence of two superconducting packings of the same electronically active unit reveals that T_c scales universally in a structure-independent dome-like relationship with proximity to the Mott metal–insulator transition, which is governed by the role of electron correlations characteristic of high-temperature superconducting materials other than fullerides.

The f.c.c. Cs_3C_{60} polymorph (Fig. 1a), in coexistence with the majority b.c.c.-packed A15 phase, was first identified as a minor component of the phase assemblage in our earlier low-temperature synthetic work using methylamine as the solvent medium[5]. Samples containing fractions as high as 86% of f.c.c. Cs_3C_{60} and minimal amounts of A15 Cs_3C_{60} (~3%) can now be accessed by a multistep procedure, which first involves reaction between stoichiometric amounts of Cs and C_{60} in liquid ammonia, followed by removal of ammonia under vacuum and controlled thermal treatment. Formation of the more stable A15 b.c.c.-packed compound and of competing fullerides with other anion charges is further minimized by exposure of the intermediate to methylamine vapour, followed by additional thermal treatment at high temperature (Supplementary Scheme 1).

Rietveld analysis of high-resolution synchrotron X-ray powder diffraction data (Fig. 1b) confirms the Cs_3C_{60} composition (refined stoichiometry, $Cs_{2.901(6)}C_{60}$), with the highest reported lattice parameter for an f.c.c. A_3C_{60} fulleride of 14.76151(8) Å and volume per anion of $V = 804.14(1)$ Å^3 per C_{60}^{3-} at ambient temperature and pressure (estimated standard deviations in the last digits are given in parentheses). Complementary Raman spectroscopy measurements are consistent with an oxidation state of −3 for the C_{60} units (Supplementary Fig. 1a). In contrast to the b.c.c.-structured A15 polymorph (Supplementary Fig. 1b), the fulleride anions are orientationally disordered in space group $Fm\bar{3}m$. Face-centred cubic Cs_3C_{60} remains strictly cubic to low temperatures (Supplementary Figs 2b, 3a).

Magnetization measurements on materials with a high f.c.c. phase fraction (86%) reveal that, in contrast to all previous f.c.c. A_3C_{60} phases, f.c.c. Cs_3C_{60} is not superconducting at ambient pressure. Though the multiphase nature of the sample requires quantitative analysis of the normal state magnetic susceptibility to be treated with caution, the observation at high temperature of Curie–Weiss behaviour with a negative Weiss temperature (−105(2) K) and moments per anion ($\mu_{eff} = 1.614(4)\mu_B$) similar to those in the localized electron A15 material ($\mu_{eff} \approx 1.3\mu_B$)[6] suggest a localized electron ground state with antiferromagnetic correlations. (Here μ_B is the Bohr magneton.) However, the temperature dependence of the magnetic susceptibility, χ, measured down to 2 K provides no evidence for a transition to an antiferromagnetically ordered state, in contrast to the cusp in $\chi(T)$ observed for the b.c.c.-based A15 polymorph at 46 K (Fig. 2a and Supplementary Fig. 4). We used NMR and muon spin relaxation as local probes to establish definitively the role of the changed lattice packing on the ambient pressure magnetic properties of f.c.c. Cs_3C_{60}.

NMR spectroscopy allows the examination of the electronic behaviour of the separate phases within the sample, as each gives rise to distinct resonances[6,7]. In metallic f.c.c. A_3C_{60} materials, the inverse of ^{13}C spin–lattice relaxation time, $1/^{13}T_1$, varies quasi-linearly with temperature owing to the Korringa relaxation of the nuclear spins by the conduction-electron spins[8]. In striking contrast, in f.c.c. Cs_3C_{60}, $1/^{13}T_1$ is almost temperature independent between 400 and 100 K (Fig. 2b). This shows that the heavily expanded f.c.c. Cs_3C_{60} is not a simple Fermi liquid, and is instead an exchange-coupled antiferromagnetic insulator at ambient pressure. In such a system, $\frac{1}{^{13}T_1} = \sqrt{2\pi}\left(A^2 + \frac{1}{2}A_{dip}^2\right)\frac{S(S+1)}{3\omega_{ex}}$, where typical values for C_{60}^{3-} are 0.69 MHz for the hyperfine coupling constant, $A/2\pi$, and 3.38 MHz

[1]Department of Chemistry, University of Liverpool, Liverpool L69 7ZD, UK. [2]Department of Chemistry, Durham University, Durham DH1 3LE, UK. [3]Institute Jožef Stefan, Jamova 39, 1000 Ljubljana, Slovenia. [4]Faculty of Mathematics and Physics, University of Ljubljana, Jadranska 19, 1000 Ljubljana, Slovenia. [5]ISIS Pulsed Neutron and Muon Source, STFC Rutherford Appleton Laboratory, Didcot OX11 0QX, UK. [6]Japan Synchrotron Radiation Research Institute, SPring-8, Hyogo 679-5198, Japan. [7]RIKEN SPring-8 Center, Hyogo 679-5148, Japan. *These authors contributed equally to this work.

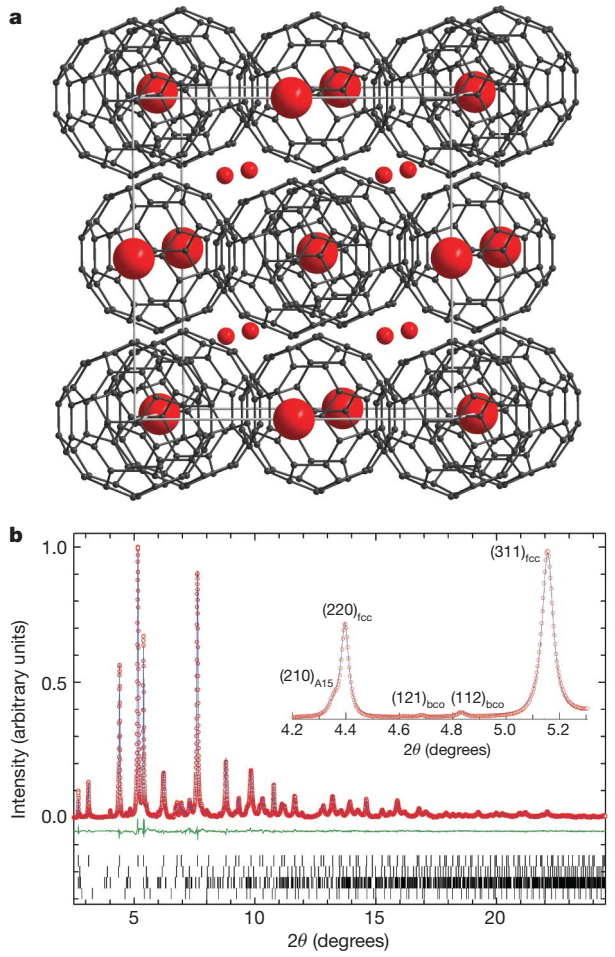

Figure 1 | Crystal structure and structural characterization of f.c.c. Cs_3C_{60}. **a**, The crystal structure of f.c.c. Cs_3C_{60} (ORTEP representation). The C_{60}^{3-} anions (carbon, dark grey) are orientationally disordered—only one orientation is shown for clarity. The mean C_{60}^{3-}–C_{60}^{3-} near-neighbour contacts (3.59 Å through neighbouring hexagon:pentagon C–C bonds) are markedly shorter than those in the lower-anion-density (817.9 Å^3 per C_{60}^{3-}) A15 polymorph (3.80 Å through hexagon:hexagon faces: Supplementary Fig. 1b). The mean Cs…C distance (3.45 Å) for the tightly coordinated tetrahedral site of f.c.c. Cs_3C_{60} is shorter than that in A15 Cs_3C_{60} (3.66 Å). The more spacious octahedral Cs site in f.c.c. Cs_3C_{60} supports a more expanded coordination environment—mean Cs…C distance, 3.90 Å. In common with all f.c.c. A_3C_{60} phases[20], the Cs^+ ion residing in the large octahedral interstices displays a very large isotropic thermal parameter, B_{iso} (=11.65(7) Å^2), corresponding to a mean square fluctuation about the centre of the hole, $\sqrt{\langle u^2\rangle}$ = 0.665(2) Å. On cooling, the Debye–Waller factor decreases smoothly to low temperatures where considerable disorder (presumably of static origin) still persists ($\sqrt{\langle u^2\rangle}$ = 0.373(1) Å at 30 K) (Supplementary Fig. 2a). The Cs cations (red) residing in the tetrahedral and octahedral interstices are shown with 90% thermal ellipsoids to emphasize this disorder, which is absent in A15 Cs_3C_{60} where the Cs ions reside in less spacious distorted tetrahedral holes. **b**, Main panel, final observed (red) and calculated (blue line) synchrotron X-ray (λ = 0.40004 Å) powder diffraction profile for the f.c.c.-rich sample (85.88(2)%) at ambient temperature. The lower line (green) shows the difference profile, and the ticks show the reflection positions of the f.c.c. (top), A15 (3.31(5)%, upper middle), body-centred orthorhombic (b.c.o.) (6.7(2)%, lower middle), and CsC_{60} (4.10(6)%, bottom) phases—refined parameters and agreement indices are given in Supplementary Table 1. Inset, expanded view of the diffraction profile (4.2-5.3°) with the observed reflections labelled by their (*hkl*) Miller indices.

for the dipolar hyperfine coupling constant, $A_{dip}/2\pi$ (ref. 9). The experimental value of $1/^{13}T_1$ (18(1) s^{-1}) is well reproduced by this formula when using an exchange frequency, $\omega_{ex} = [2zk_B{}^2J^2S(S+1)/3\hbar^2]^{1/2}$, calculated with an exchange constant J = 30 K (ref. 7) and assuming the low-spin state, S = ½, consistent with the magnetization data, suggesting similar strength exchange interactions with the A15 polymorph.

Both relaxation rates $1/^{13}T_1$ and $1/^{13}T_2$ (T_2 is the ^{13}C spin–spin relaxation time) start to increase below ~15 K (Fig. 2b, c). This gives a strong indication that the local fields experienced by the ^{13}C probe begin to freeze gradually below this temperature. This is also reflected in the increase of the total second moment, $^{133}M_2$, of the ^{133}Cs NMR resonances (Fig. 2d, e). The temperature dependence of $^{133}M_2{}^{1/2}$ below 15 K is not consistent with the onset of long-range antiferromagnetic ordering with well defined T_N, as found in A15 Cs_3C_{60}, where T_N = 46 K is signalled by a steep increase in $^{133}M_2{}^{1/2}$ (refs 6, 7).

Zero-field muon spin relaxation (ZF-μ^+SR) shows gradual freezing of the paramagnetic spin fluctuations in f.c.c. Cs_3C_{60} below 18 K. Quasi-static local magnetic fields, whose fraction grows with decreasing temperature, gradually develop and co-exist with paramagnetic local fields down to 2.5 K. At even lower temperatures, the ZF-μ^+SR spectra change drastically and are dominated by a heavily damped spontaneous muon precession (Fig. 2f). At 0.52 K, the ZF μ^+-spin precession frequency, ν_μ, is 0.205(2) MHz, corresponding to a static local field at the μ^+ site of $\langle B_\mu\rangle$ = 15.1(1) G. This is smaller by a factor of 3 than the values observed for the A15-structured Cs_3C_{60} (ref. 6) and the $(NH_3)K_3C_{60}$ (ref. 10) antiferromagnets. The appearance of this oscillating signal demonstrates the existence of coherent ordering of the electronic C_{60}^{3-} spins (on the length scale probed by the muons) throughout the whole sample volume, and underlines the long-range antiferromagnetic ordering below T_N of 2.2 K (Fig. 2g). We note that the very strong oscillation damping is the signature of severe spatial disorder and inhomogeneity effects—at 0.52 K, the width of the local field distribution, $\langle\Delta B^2\rangle^{1/2}$ = 12.8(1) G, is comparable to the magnitude of the static local fields at the μ^+ sites. The quasi-static nature of the highly disordered local magnetic fields is confirmed by the complete recovery of the asymmetry in a longitudinal field of 100 Oe (Supplementary Fig. 8).

Magnetization measurements under pressure reveal that f.c.c. Cs_3C_{60} becomes superconducting on the application of moderate applied pressures (Fig. 3a). Superconductivity (with a broad diamagnetic response at the trace level of ~0.1%) is initially observed at 25.6 K under 1.3 kbar. Bulk superconductivity (shielding fraction ~12%) is established at 2.2 kbar with a rapidly increasing T_c of 29.7 K. This rises to a maximum of 35 K (lower than the 38 K T_c found for the b.c.c.-based A15 polymorph, Supplementary Fig. 10) at ~7 kbar, before decreasing to 33 K at the highest pressure studied. The resulting variation of T_c with pressure shows a rather broad maximum (Fig. 3b). Synchrotron X-ray powder diffraction measurements at the pressures used in the magnetization measurements and at temperatures below the observed T_c show that the f.c.c. structure is preserved at all temperatures and pressures relevant to the measurements discussed (Supplementary Fig. 11). The low-temperature, high-pressure diffraction results (Fig. 3c) allow the superconducting T_c to be related to the C_{60} packing density measured by V. After peaking at 35 K for V = 759.6 Å^3 per C_{60}^{3-}, the $T_c(V)$ dependence at the highest pressures (lowest volumes) correlates well with that observed for the less expanded f.c.c. A_3C_{60} superconductors at ambient pressure[11] (Fig. 4a).

Superconductivity emerges out of the insulating state at a critical value of V = 786.0 Å^3 per C_{60}^{3-}, smaller than that for A15 Cs_3C_{60} (at 796.6 Å^3 per C_{60}^{3-}). Observation of the packing densities at which the metal–insulator transition takes place allows us to estimate the bare bandwidth, W_c, at which the metallic state becomes unstable (Fig. 4b inset). W_c evaluated in this way[12] is ~0.35 eV for f.c.c. and ~0.55 eV for b.c.c. lattices, consistent with the lattice topology controlling the metal–insulator transition as proposed in ref. 13—intriguingly, the ratio of W_c in the two sphere packings is 1.6 experimentally, which compares well with the prediction of 1.8. The f.c.c. packing thus stabilizes metallic states to much smaller W than does b.c.c.

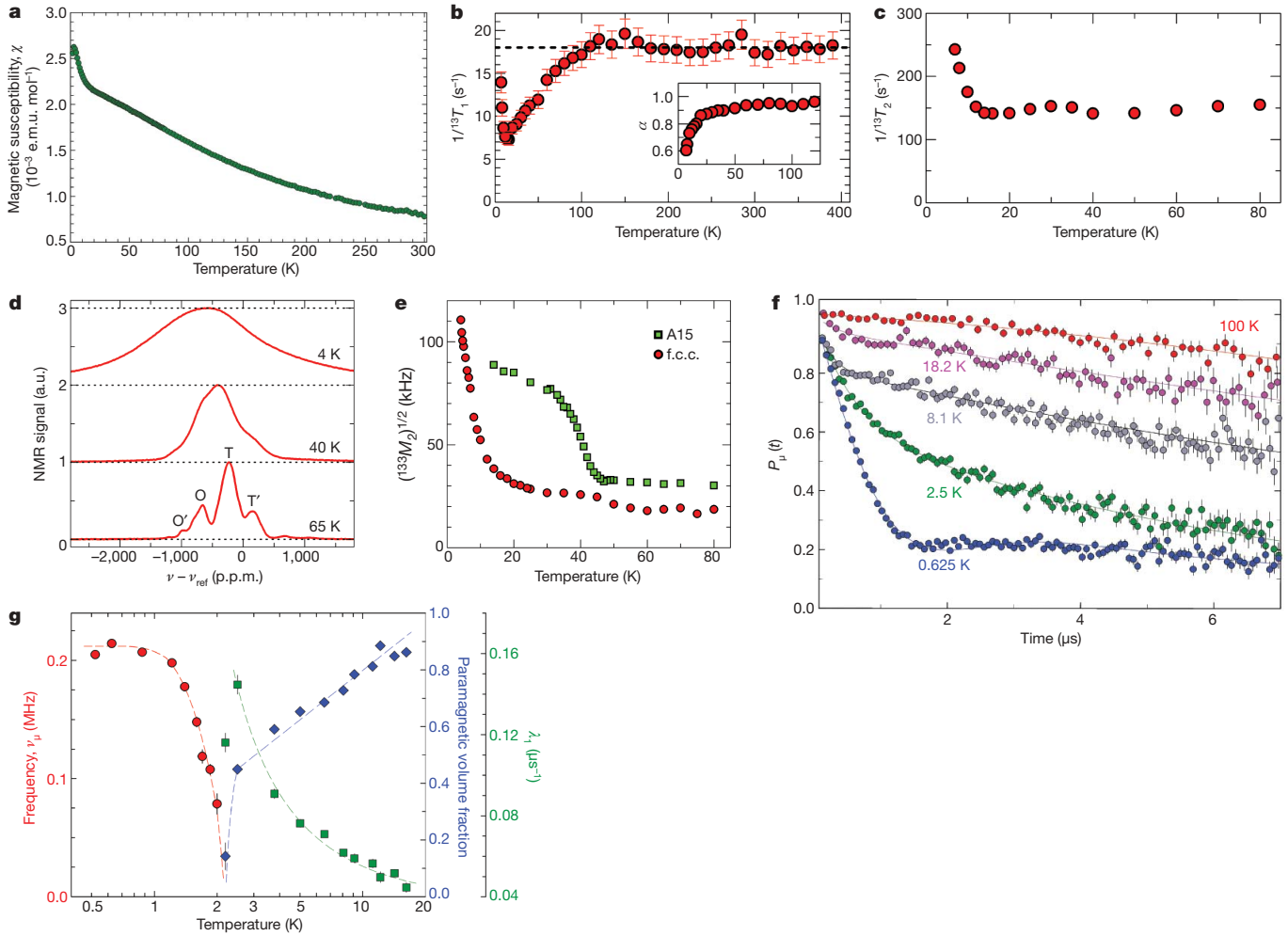

Figure 2 | Ambient pressure magnetic properties of f.c.c. Cs_3C_{60}. **a**, Temperature dependence of the magnetic susceptibility, $\chi(T)$ (green circles), of f.c.c.-rich Cs_3C_{60}, obtained from the difference of the values at 5 T and 3 T. **b**, Temperature dependence of the spin–lattice relaxation rate, $1/^{13}T_1$. Inset, below 100 K, there is a distribution of relaxation rates, giving stretched-exponential behaviour to the ^{13}C magnetization relaxation curves, $M_z(\tau) - M_z(0) \propto \exp[-(\tau/T_1)^{\alpha}]$, where $M_z(\tau)$ is the z-component of the nuclear spin magnetization measured at time τ after a train of pulses saturated the ^{13}C nuclear spin magnetization. The stretch exponent α changes below ~15 K. **c**, Temperature dependence of the spin–spin relaxation rate, $1/^{13}T_2$. Gradual freezing of local magnetic moments gives a rapid increase below 15 K. **d**, ^{133}Cs NMR spectra of f.c.c. Cs_3C_{60} between 4 and 65 K. O and T are resonances for the octahedral and tetrahedral sites, T′ and O′ are associated with the anion disorder[21]. **e**, Temperature dependence of the second moment, $^{133}M_2^{1/2}$ (red circles). Its increase at low T is ascribed to the increased width of the distribution of static local magnetic fields (see also Supplementary Fig. 7). For comparison, we show $^{133}M_2^{1/2}$ in A15 Cs_3C_{60} ($T_N = 46$ K). **f**, Temperature evolution of the ZF μ^+-spin polarization, $P_\mu(t)$, for f.c.c.-rich Cs_3C_{60} between 0.625 and 100 K. At high temperatures, the spectra imply the presence of weak static nuclear moments together with a slow relaxation arising from fluctuating electronic moments. Between 16.2 and 2.5 K, they are consistent with inhomogeneous magnetism: that is, co-existing spin frozen and paramagnetic domains. Below 2.2 K, they are dominated by a short-lived heavily damped oscillating signal. **g**, Temperature evolution of the ZF μ^+-spin precession frequency, ν_μ, below $T_N \approx 2.2$ K, and of the volume fraction and relaxation rate, λ_1, of the slowly relaxing (paramagnetic) component for temperatures where paramagnetic and spin frozen domains coexist. The lines through the points are guides to the eye. a.u., arbitrary units. Error bars, ±s.d.

The different sphere packings in the f.c.c. and A15 b.c.c.-based Cs_3C_{60} polymorphs produce distinct dome-like $T_c(V)$ relationships (Fig. 4a). Within each polymorph, the packing density measured by V represents the ratio of the on-site interelectron repulsion, U, to the bare bandwidth, W, which controls the Mott metal–insulator transition, as expansion reduces W. The superconducting and metallic states are stable at higher V in the less dense b.c.c.-based A15 than the f.c.c. polymorph. At the same V, the b.c.c.-based polymorph has a higher T_c, consistent with band structure calculations[12] that show that at a given V, the A15 phase has a higher density of states at the Fermi level, $N(E_F)$. The bandwidths W in the A15 phase are also higher, allowing the metallic state to remain stable to larger V than is possible in the f.c.c. phase. The sphere packing adopted in each of the two Cs_3C_{60} polymorphs thus controls the superconducting T_c through the different intermolecular overlaps in the two cases. The larger W and higher $N(E_F)$ in the b.c.c. packing, in combination with orientationally ordered anions and considerably reduced static positional disorder on the Cs positions, give a higher T_c.

As W_c is controlled by the lattice packing (Supplementary Fig. 12), we can use this parameter to scale T_c in the two polymorphs by replacing V—which represents U/W within each polymorph but does not allow direct comparison between sphere packings—with $(U/W)/(U/W)_c = (W_c/W)$. Both Cs_3C_{60} polymorphs have the same dependence of T_c on this reduced variable, showing that T_c is controlled by proximity to the metal–insulator transition, independent of the sphere packing adopted. The maximum T_c in both cases occurs when $(W_c/W) \approx 0.87$, and normalization to the maximum T_c in each family maps all of the bcc and f.c.c. C_{60}^{3-} superconductors onto a single packing-independent universal curve (Fig. 4b), suggesting the same pairing mechanism in both cases, controlled by proximity to the metal–insulator transition. Further band narrowing towards the metal–insulator transition from this point inverts the relationship

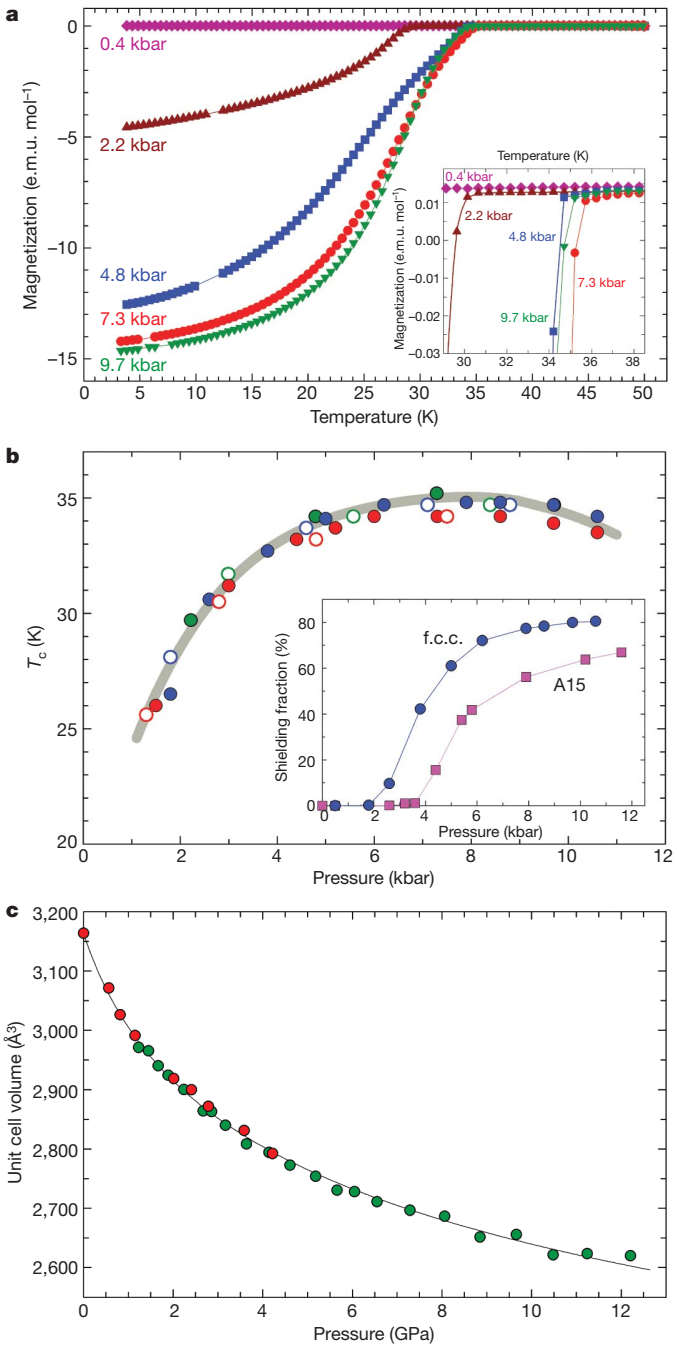

Figure 3 | Superconductivity under pressure in f.c.c. Cs_3C_{60}. **a**, Temperature dependence of the magnetization, M (ZFC protocol, 20 Oe), at selected pressures. Inset, expanded view of the data near the onset of the metal-to-superconductor transition, T_c. FC and ZFC data confirming the Meissner effect are shown in Supplementary Fig. 9. **b**, Pressure dependence of T_c measured for three different f.c.c. Cs_3C_{60} samples (blue/green/red circles). Filled (open) circles label data obtained with increasing (decreasing) pressure. T_c is defined as the temperature at which $M(T)$ in **a** begins to decrease. Inset, evolution of the shielding fraction with change in pressure. The data for A15 Cs_3C_{60} (squares) are also included[5] to emphasize the lower pressure onset of bulk superconductivity in the f.c.c. polymorph. **c**, Pressure dependence of the unit cell volume of the f.c.c. Cs_3C_{60} phase at 15 K up to an applied pressure of 13 GPa (different colours indicate different sample batches). A linear fit to the data up to 0.8 GPa gives a volume compressibility, $\kappa = 0.053(1)\ \mathrm{GPa}^{-1}$, comparable to that measured for A15 Cs_3C_{60} ($\kappa = 0.054(5)\ \mathrm{GPa}^{-1}$)[6]. The line through the data points is a least-squares fit to the second-order Murnaghan equation of state, with an atmospheric pressure isothermal bulk modulus (K_0) of 13.7(3) GPa, and its pressure derivative $K'_0 = 13.0(3)$.

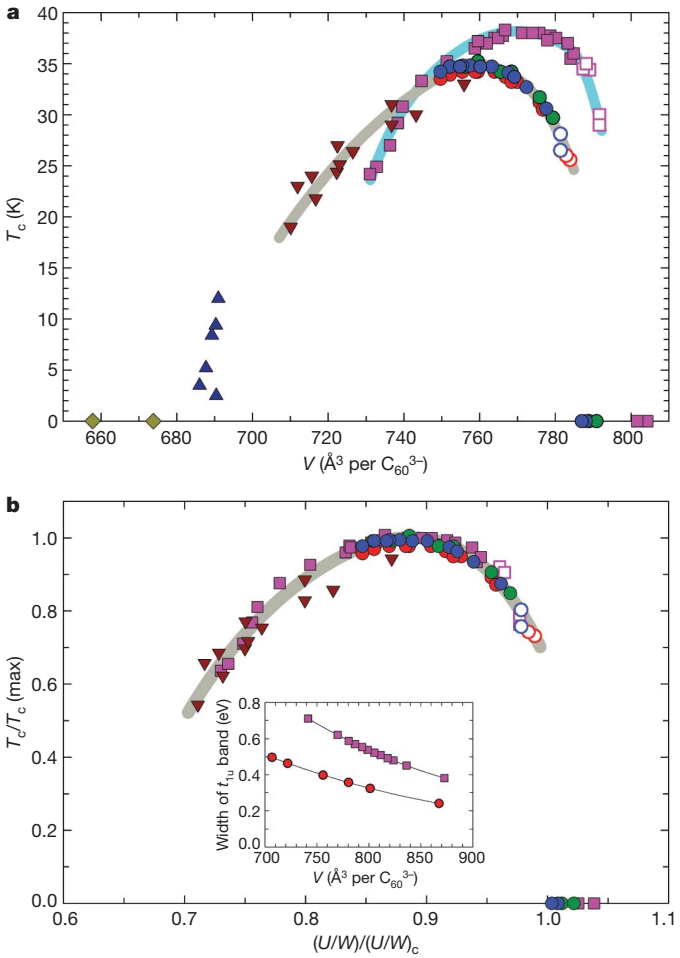

Figure 4 | Electronic phase diagrams shown as functions of volume occupied per fulleride anion and normalized conduction bandwidth in the two sphere packings of A_3C_{60} superconductors. **a**, Superconducting transition temperature, T_c, as a function of volume occupied per fulleride anion, V, at low temperature. The red/green/blue circles and pink squares correspond to the bulk $T_c(V)$ behaviour observed in f.c.c.- and A15-structured Cs_3C_{60}, respectively. Open symbols represent data at pressures where trace superconductivity is observed and where in the A15 phase superconductivity coexists with antiferromagnetism. The yellow rhombi, dark blue triangles and brown inverted triangles correspond to the ambient pressure T_c of f.c.c. C_{60}^{3-} anion packings with Li_2CsC_{60}, $Pa\bar{3}$ symmetry, and $Fm\bar{3}m$ symmetry, respectively. **b**, Normalized superconducting transition temperature, $T_c/T_c(\mathrm{max})$, as a function of the ratio (U/W) divided by the critical value $(U/W)_c$ required to produce localization in the A_3C_{60} fulleride structures with f.c.c.- and bcc-sphere packings. W_c is estimated as 0.55 eV for b.c.c.-structured A15 Cs_3C_{60} and 0.35 eV for the f.c.c. phases. The symbols have the same meaning as in **a**. Inset, dependence of the t_{1u} conduction bandwidth on volume occupied per fulleride anion, V, for f.c.c.-sphere (red circles) and b.c.c.-sphere (pink squares) packings, as determined by electronic structure calculations[12].

between $N(E_F)$ and T_c—this is assigned to fluctuations associated with the magnetic insulating ground state for each polymorph. In the case of A15, this is the antiferromagnetic long-range ordered state (T_N is 46 K and increases with pressure), whereas in the geometrically frustrated f.c.c. case, it is a strongly coupled but disordered paramagnet where both structural and magnetic disorder play an important role (the lowest measured f.c.c. T_c is above both the magnetic freezing and ordering temperatures seen by NMR and muons).

Both Cs_3C_{60} polymorphs have long-range cubic symmetry, and thus retain the key C_{60}^{3-} molecular property of frontier orbital degeneracy[14,15], which underpins the competing cooperative electronic states of superconductivity and magnetic order[16,17]. Within the cubic symmetry, the lattice packing of the C_{60}^{3-} unit controls the onset temperatures of both of these states. The geometrical frustration of

the f.c.c. lattice[18] gives a magnetic ordering temperature an order of magnitude lower than that found for the non-frustrated b.c.c.-based packing—the anion orientational disorder in the f.c.c. case suppresses the frustration and allows access to the ordered state at low temperature. The superconducting T_c in each polymorph is controlled by the proximity to the metal–insulator transition and thus by the critical electronic bandwidth, W_c, for electron correlation-driven localization that is also controlled by each distinct packing motif. This permits a scaling of the two distinct $T_c(V)$ relationships onto a single dome-shaped universal curve, suggesting that it is the separation from the competing localized electron ground state that determines T_c in fullerides, with the absolute values observed depending on the details of the molecular overlap within the two different sphere packings. Electron correlations are also important in high-T_c superconductors like the copper oxides[1], where the packing of the electronically active ions is essentially identical (two-dimensional square) in all known superconducting families. Cs_3C_{60} is unique, as the same electronically active unit can be packed in two distinct lattice motifs to reveal that T_c scales in a lattice-independent manner with proximity to the correlation-driven Mott metal–insulator transition.

During the review process of this manuscript, a preprint appeared on the arXiv server[19] reporting NMR results that partially overlap with those presented here.

METHODS SUMMARY

All samples synthesized are highly air sensitive, so great care was taken to ensure the sample environment was meticulously clean, dry and air free. Numerous samples were prepared in the course of our synthetic exploration (variation in solvent used, annealing protocols), which was aimed at optimizing the content of f.c.c. Cs_3C_{60} and minimizing that of A15 Cs_3C_{60} in the resulting phase assemblages. The outcome of each step of the reaction procedure was monitored by powder X-ray diffraction on samples sealed in 0.5-mm glass capillaries under He or Ar atmospheres. The synthetic procedure that produced the maximum content of the f.c.c. Cs_3C_{60} polymorph is described in the Methods section.

Synchrotron X-ray diffraction data were collected at temperatures between 295 and 12 K using the high-resolution powder diffractometers on beamline ID31 at the European Synchrotron Radiation Facility (ESRF), Grenoble, and on beamline I11 at the Diamond synchrotron, UK. Low-temperature high-pressure synchrotron X-ray diffraction experiments were performed in a diamond anvil cell at SPring-8, Japan, at beamline BL10XU. Data analysis of the diffraction profiles was performed with the GSAS suite of Rietveld programs.

Magnetization measurements were performed under both zero-field-cooling (ZFC) and field-cooling (FC) protocols with a Quantum Design SQUID magnetometer. Hydrostatic external pressure to 10.6 kbar was applied with a piston-cylinder high pressure cell (easyLab Technologies Mcell10) using high-purity Sn as an *in situ* manometer. Zero-field (ZF) and longitudinal-field (LF) μ^+SR data were collected at ISIS, Rutherford Appleton Laboratory, with the MuSR spectrometer. Experiments were performed in the temperature range between 1.4 and 100 K using a continuous-flow helium cryostat and between 0.52 and 2 K using a ^{3}He sorption cryostat. ^{133}Cs (spin $I = 7/2$) and ^{13}C (spin $I = ½$) NMR spectra, spin–lattice relaxation time, T_1, and spin–spin relaxation time, T_2, were measured between 4 and 400 K (T_2 measurements to 80 K) at a magnetic field of 9.39 T. All experimental procedures and analysis are described in detail in the Methods section.

Full Methods and any associated references are available in the online version of the paper at www.nature.com/nature.

Received 24 March; accepted 27 April 2010.
Published online 19 May 2010.

1. Lee, P. A., Nagaosa, N. & Wen, X. G. Doping a Mott insulator: physics of high-temperature superconductivity. *Rev. Mod. Phys.* **78,** 17–85 (2006).
2. Hebard, A. F. *et al.* Superconductivity at 18 K in potassium-doped C_{60}. *Nature* **350,** 600–601 (1991).
3. Tanigaki, K. *et al.* Superconductivity at 33 K in $Cs_xRb_yC_{60}$. *Nature* **352,** 222–223 (1991).
4. Palstra, T. T. M. *et al.* Superconductivity at 40 K in cesium doped C_{60}. *Solid State Commun.* **93,** 327–330 (1995).
5. Ganin, A. Y. *et al.* Bulk superconductivity at 38 K in a molecular system. *Nature Mater.* **7,** 367–371 (2008).
6. Takabayashi, Y. *et al.* The disorder-free non-BCS superconductor Cs_3C_{60} emerges from an antiferromagnetic insulator parent state. *Science* **323,** 1585–1590 (2009).
7. Jeglič, P. *et al.* Low-moment antiferromagnetic ordering in triply charged cubic fullerides close to the metal-insulator transition. *Phys. Rev. B* **80,** 195424 (2009).
8. Pennington, C. H. & Stenger, V. A. Nuclear magnetic resonance of C_{60} and fulleride superconductors. *Rev. Mod. Phys.* **68,** 855–910 (1996).
9. Sato, N. *et al.* Analysis of ^{13}C-NMR spectra in C_{60} superconductors: hyperfine coupling constants, electronic correlation effect, and magnetic penetration depth. *Phys. Rev. B* **58,** 12433–12440 (1998).
10. Prassides, K. *et al.* Magnetic ordering in the ammoniated fulleride $(ND_3)K_3C_{60}$. *J. Am. Chem. Soc.* **121,** 11227–11228 (1999).
11. Tanigaki, K. & Zhou, O. Conductivity and superconductivity in C_{60} fullerides. *J. Phys. I* **6,** 2159–2173 (1996).
12. Darling, G. R., Ganin, A. Y., Rosseinsky, M. J., Takabayashi, Y. & Prassides, K. Intermolecular overlap geometry gives two classes of fulleride superconductor: electronic structure of 38 K T_c Cs_3C_{60}. *Phys. Rev. Lett.* **101,** 136404 (2008).
13. Gunnarsson, O., Han, J. E., Koch, E. & Crespi, V. H. Superconductivity in alkali-doped fullerides. *Struct. Bond.* **114,** 71–101 (2005).
14. Gunnarsson, O., Koch, E. & Martin, R. M. Mott transition in degenerate Hubbard models: application to doped fullerenes. *Phys. Rev. B* **54,** R11026–R11029 (1996).
15. Gunnarsson, O. Superconductivity in fullerides. *Rev. Mod. Phys.* **69,** 575–606 (1997).
16. Capone, M., Fabrizio, M., Castellani, C. & Tosatti, E. Strongly correlated superconductivity. *Science* **296,** 2364–2366 (2002).
17. Capone, M., Fabrizio, M., Castellani, C. & Tosatti, E. Modelling the unconventional superconducting properties of expanded A_3C_{60} fullerides. *Rev. Mod. Phys.* **81,** 943–958 (2009).
18. Wiebe, C. R. *et al.* Frustration-driven spin freezing in the S=1/2 fcc perovskite Sr_2MgReO_6. *Phys. Rev. B* **68,** 134410 (2003).
19. Ihara, Y. *et al.* NMR study of the Mott transitions to superconductivity in the two Cs_3C_{60} phases. Preprint at ⟨http://arxiv.org/abs/1003.2937⟩ (2010).
20. Bendele, G. M., Stephens, P. W. & Fischer, J. E. Octahedral cations in Rb_3C_{60}: reconciliation of conflicting evidence from different probes. *Europhys. Lett.* **41,** 553–558 (1998).
21. Walstedt, R. E., Murphy, D. W. & Rosseinsky, M. J. Structural distortion in rubidium fulleride (Rb_3C_{60}) revealed by ^{87}Rb NMR. *Nature* **362,** 611–613 (1993).

Supplementary Information is linked to the online version of the paper at www.nature.com/nature.

Acknowledgements We thank EPSRC for support (EP/G037132 and EP/G037949) and STFC for access to the synchrotron X-ray facilities at the ESRF (where we thank A. N. Fitch for assistance on beamline ID31) and Diamond (where we thank C. Tang for assistance on beamline I11) and to the muon facilities at ISIS. We also thank SPring-8 for access to the synchrotron X-ray facilities.

Author Contributions M.J.R. and K.P. directed and coordinated the project. A.Y.G., M.T.M., M.D.T. and A.M. synthesized the samples. Y.T., A.Y.G. and K.P. performed the ambient pressure synchrotron XRD measurements and Y.T. analysed the data. Y.T., M.T.M. and M.D.T. carried out the ambient and high pressure magnetization measurements. Y.T., A.Y.G., Y.O., M.T. and K.P. performed the high pressure synchrotron XRD measurements and Y.T. analysed the data. Y.T., A.Y.G., P.J.B. and K.P. carried out the μSR measurements and K.P. and P.J.B. analysed the data. P.J., A.P. and D.A. performed and analysed the NMR measurements. G.R.D. carried out electronic structure calculations. M.J.R. and K.P. wrote the paper. All authors commented on the paper.

Author Information Reprints and permissions information is available at www.nature.com/reprints. The authors declare no competing financial interests. Readers are welcome to comment on the online version of this article at www.nature.com/nature. Correspondence and requests for materials should be addressed to M.J.R. (M.J.Rosseinsky@liverpool.ac.uk) or K.P. (K.Prassides@durham.ac.uk).

METHODS

Synthesis of f.c.c. Cs_3C_{60} samples. In a glove box ($H_2O < 0.1$ p.p.m., $O_2 < 0.1$ p.p.m.), reaction mixtures of 165.5 mg (1.245 mmol) of Cs (99.95% Aldrich, resublimed) and 298.8 mg (0.415 mmol) of C_{60} (99.9% MER, resublimed) were placed in a glass vessel along with a magnetic stirring bar. The vessel was removed from the glove box, linked to an ammonia-containing vessel on a high vacuum manifold and the system was evacuated to 10^{-4} torr. Condensation of 60 ml of liquid ammonia (pre-dried by condensation onto sodium at −65 °C) into the reaction vessel at −70 °C afforded a brown solution. After 20 min, the solution was slowly (~2 °C min^{-1}) warmed to ~22.5 °C while stirring (300 r.p.m.). The vessel was sealed while stirring continued for another 30 min. Following re-condensation, the vessel with liquid ammonia was sealed and preserved for subsequent synthesis. The damp product was evacuated to a pressure of 10^{-1} torr. 413 mg of the precursor **A** (CHN analysis: $(NH_3)_{1.2(1)}Cs_{3.1(1)}C_{60}$) was removed from the reaction vessel in the glove box and ground using pestle and mortar.

A sample of **A** (399.6 mg) was loaded into a 12-mm Pyrex tube, attached to a high vacuum line and annealed under dynamic vacuum for 16 h in a tube furnace (room temperature to 130 °C at 5 °C min^{-1}; held for 6 min; to 120 °C at 5 °C min^{-1}; held for 16 h; to room temperature at 5 °C min^{-1}) to afford 379.6 mg of precursor **B** (CHN analysis: $(NH_3)_{0.1(1)}Cs_{3.1(1)}C_{60}$).

A sample of **B** (358.4 mg) was loaded into a Ta cell. The cell was sealed inside a glass ampoule under He gas pressure (130 torr) and heated inside a furnace (room temperature to 405 °C at 2 °C min^{-1}; held for 84 h; to room temperature at 2 °C min^{-1}). After the completion of heat treatment, the ampoule was taken to the glove box, affording 358 mg of precursor **C** (CHN analysis: $Cs_{3.1(1)}C_{60}$).

A sample of **C** (296.0 mg) was loaded into a glass vessel. The vessel was removed from the glove box, linked to a vessel containing liquid methylamine (pre-dried by condensation onto sodium at −65 °C) on a high vacuum manifold, and the system was evacuated to 10^{-4} torr. Precursor **C** was then exposed to methylamine vapour at ~22.5 °C. After 15 min of reaction with methylamine vapour, the vessel was sealed and allowed to settle at room temperature for 60 min. The damp product was dried by opening the reaction vessel to 10^{-2} torr using a rotary pump and then to 6×10^{-5} torr using a turbomolecular pump. Finally, the reaction vessel was annealed with a heat gun at 180 °C.

The product (286 mg) was removed from the vessel inside the glove box and subsequently sealed under a He gas pressure of 300 torr into an 8-mm silica ampoule. The ampoule was placed into a furnace, heated to 405 °C at 5 °C min^{-1}, and after 18 h heating, returned to ambient temperature to afford 278 mg of the final product sample **1** (CHN analysis: $Cs_{3.1(1)}C_{60}$). The reaction sequence is represented in Supplementary Scheme 1. An additional sample **5** was also prepared according to the same synthetic protocol. The high annealing temperatures (405 °C) used in these reactions, together with the sequential use of ammonia and methylamine solvents, have proven crucial in the isolation of f.c.c.-rich assemblages. This contrasts with the preferential formation of the A15 phase that forms at much lower annealing temperatures from methylamine-containing precursors[6].

The composition of the phase assemblage in various batches—synthesized by a simpler procedure of reacting Cs and C_{60} in either liquid ammonia (sample **2**) or methylamine (samples **3** and **4**) followed by removal of the solvent under vacuum and thermal treatment and summarized in Supplementary Table 2—was determined by Rietveld refinements of high-resolution synchrotron X-ray powder diffraction data collected at ambient temperature using the high-resolution powder diffractometers on beamline ID31 at the ESRF and I11 at Diamond (sample **1**: $\lambda = 0.40004$ Å; sample **2**: $\lambda = 0.39988$ Å; sample **3**: $\lambda = 0.40289$ Å; sample **4**: $\lambda = 0.40289$ Å; sample **5**: $\lambda = 0.82603$ Å). Diffraction data were also collected as a function of temperature between 295 and 30 K for sample **1** (ID31, $\lambda = 0.40004$ Å) and at 12 K for sample **2** (I11, $\lambda = 0.82603$ Å). Rietveld analysis was performed with the GSAS suite. Representative results of the structural analysis are shown in Fig. 1b and Supplementary Fig. 3 for samples **1** and **5**.

Raman spectroscopy. Raman spectra of samples **1** and **5** were collected at ambient temperature using a 514.5-nm laser with a JY LabRam-HR Spectrometer operated in back-scattered geometry over a sample area of 500 μm^2. The typical acquisition times were 20 × 6 s. Calibration was performed by referencing the spectrometer to the 520.07 cm^{-1} silicon line. C_{60} and Cs_6C_{60} samples were used as standards ($A_g(2)$ peaks at 1,468 and 1,430 cm^{-1}, respectively). The resulting Raman mode shift per one electron transferred to C_{60} is ~6.33 cm^{-1}. The $A_g(2)$ mode of samples **1** and **5** is observed at 1,449 cm^{-1} (Supplementary Fig. 1a), confirming the 3− oxidation state of C_{60}.

Magnetic measurements. Temperature-dependent magnetic susceptibility, χ, measurements at ambient pressure were performed on ~50 and 20 mg samples (sample **1** and **5**), respectively at 3 and 5 T with a SQUID magnetometer. In order to remove the contribution of ferromagnetic impurities, $\chi(T)$ was obtained from the difference of the values at 5 and 3 T (Fig. 2a and Supplementary Fig. 4). Field-dependent magnetization, M, measurements were performed on sample **1** at selected temperatures between 1.8 and 300 K in applied fields between 0 and 5 T. M of sample **1** was also measured at 100 Oe between 1.8 and 60 K under both ZFC and FC protocols—these data show the absence in f.c.c. Cs_3C_{60} of the weak ferromagnetism observed in A15 Cs_3C_{60} (Supplementary Fig. 5). High-pressure magnetic measurements were undertaken using an easyLab Technologies piston-cylinder high pressure cell (Mcell10) with an upper limit of hydrostatic pressure of 10.6 kbar; high-purity Sn was used as an *in situ* manometer with Daphne oil as pressure transmitting medium, and magnetization data were collected on ~20-mg samples loaded in an argon-filled glovebox (samples **1**, **2** and **3**) under ZFC and FC protocols at 20 Oe.

Low-temperature high-pressure synchrotron X-ray diffraction. High-pressure synchrotron X-ray diffraction experiments were performed for samples **1** (18 K, ≤4.22 GPa) and **4** (15 K, ≤12.21 GPa) at BL10XU, SPring-8, Japan. The powder sample was loaded in a helium-gas-driven membrane diamond anvil cell (MDAC), which was equipped with a Be-Cu alloy gasket and placed inside a closed-cycle helium refrigerator. The diamond culet diameter was 600 μm and the sample was introduced in a 150-μm-deep hole made in the gasket. Helium gas (1.96 kbar) loaded in the MDAC was used as a pressure medium. The applied pressure was increased at base temperature by controlling the He gas pressure on the MDAC diaphragm with the cell inside the cryostat, and was measured with the ruby fluorescence method. The diffraction patterns ($\lambda = 0.41328$ Å (**1**) and 0.41219 Å (**4**)) were collected using a flat image plate detector (Rigaku R-AXIS IV++, 300 × 300 mm^2 area, 0.100 mm pixel size). Masking the Bragg reflections of the diamond anvil and integration of the two-dimensional diffraction images were performed with WinPIP software. Rietveld analysis of the one-dimensional diffraction profiles was performed with the GSAS suite.

^{133}Cs and ^{13}C NMR spectroscopy. ^{133}Cs (spin $I = 7/2$) and ^{13}C NMR (spin $I = ½$) spectra, spin–lattice relaxation time, T_1, and spin–spin relaxation time, T_2, were measured for sample **2** between 4 and 400 K (T_2 measurements to 80 K) at a magnetic field of 9.39 T. As references, $CsNO_3$ and tetramethylsilane (TMS) standards were used with corresponding reference frequencies, $\nu(^{133}Cs) = 52.4609$ MHz and $\nu(^{13}C) = 100.5713$ MHz, respectively. In the ^{133}Cs NMR experiments, a two-pulse echo pulse sequence (β)-τ-(β)-τ-echo was used, with a pulse length $\tau(\beta) = 4$ μs and an interpulse delay $\tau = 50$ μs. In the ^{13}C NMR lineshape measurements, a Hahn echo pulse sequence ($\pi/2$)-τ-(π)-τ-echo was used, with $\tau(\pi/2) = 5$ μs and interpulse delay $\tau = 50$ μs. For spin–lattice relaxation measurements, the saturation recovery technique was applied, while spin–spin relaxation times were determined by the Hahn-echo decay.

In f.c.c. Cs_3C_{60}, $1/^{13}T_1$ is almost temperature independent between 400 and 100 K. A small increase at ~280 K is due to the freezing out of the C_{60}^{3-} rotations (also seen as a broadening of the ^{13}C NMR resonance, Supplementary Fig. 6). Temperature-independent ^{133}Cs spin–lattice relaxation times, $1/^{133}T_1$, are also found for the O- and T-site ^{133}Cs resonances in this temperature range (Supplementary Fig. 7). Moreover, the slight increase in the second moment, $^{133}M_2^{1/2}$, at around 45 K (Fig. 2e) is due to the presence of a small fraction of A15 Cs_3C_{60} phase (also seen in the ^{133}Cs spectrum (Fig. 2d) as weak peaks on both sides of the main resonances).

^{133}Cs NMR proved to be extremely valuable tool for the investigation of structural and electronic properties of multiphase Cs_3C_{60} samples. We have argued successfully before[6,7] that the difference in site symmetries ($\bar{4}m.2$ versus 23. and $m\bar{3}$. for A15 and f.c.c. structures, respectively) can allow us to enhance individual signals by proper pulse sequence optimization. For the f.c.c. phase, both octahedral (O) and tetrahedral (T) Cs sites are of high symmetry, dictating that the electric field gradient is zero. Although the measured ^{133}Cs spectra in f.c.c. Cs_3C_{60} are in agreement with these arguments, the experimental situation is somewhat more complicated. Namely, in addition to the expected O and T lines, we observe that the T peak splits into two resonances, labelled as T and T′ peaks with an intensity ratio of ~5.5:1. This was observed for the first time in Rb_3C_{60} by Walstedt *et al.*[21], who found that the T-peak splitting appears below ~360 K. In Supplementary Fig. 7a, we compare the ^{133}Cs spectrum of f.c.c. Cs_3C_{60} with that of $RbCs_2C_{60}$ (as adopted from ref. 8) at 300 K. The excellent agreement between the two spectra (the modified intensity ratios of the peaks results from the presence of Rb^+ ions in the T sites for $RbCs_2C_{60}$) validates our current assignments. In addition, we observe that the O peak also splits into two O and O′ peaks (the O′ peak appearing as a shoulder on the low-frequency side of the spectra).

The temperature dependence of the centres of all four peaks is shown in Supplementary Fig. 7b. All peaks shift strongly with decreasing temperature. The shift of the ^{133}Cs resonance is expected to follow

$$^{133}\delta_{T,O} = \delta_{T,O}^{orb} + \frac{A_{T,O}}{\gamma_e \gamma_{Cs}} \chi_S$$

where $\delta_{T,O}^{orb}$ are the temperature independent orbital shifts, $A_{T,O}$ are the hyperfine coupling constants of the T and O sites, respectively, and γ_e and γ_{Cs} are the

electronic and Cs gyromagnetic ratios, respectively. It is clear that the electronic spin susceptibility, χ_S, does not display the weak temperature dependence expected for a simple Fermi-liquid ground state. Instead, the temperature dependence of the shifts resembles the Curie–Weiss response expected for exchange-coupled paramagnetic insulators. Detailed analysis of the temperature dependence of the ^{133}Cs NMR shifts will be given elsewhere.

The appearance of the T−T′ splitting in the ^{133}Cs NMR spectra is related to the freezing of the C_{60}^{3-} molecular motions. For f.c.c. Cs_3C_{60}, this occurs above 400 K. The ^{13}C NMR spectra remain relatively narrow below 400 K (Supplementary Fig. 6), suggesting that the C_{60}^{3-} molecular motions are of ratchet type. However, it seems that the molecular motions are relatively more complicated, most probably because of rapid reorientations around one molecular axis and occasional flips of the axis of rotation between symmetry allowed orientations. The uniaxial C_{60}^{3-} reorientations finally freeze out on the NMR timescale just around room temperature. This interpretation is supported by the temperature dependence of the ^{13}C NMR second moment, $^{13}M_2$, which increases in several steps on cooling below 400 K (Supplementary Fig. 6 inset).

Muon spin relaxation (μ^+SR) measurements. The powder sample (sample **1**) was sealed under argon in a 24-mm-diameter Ti sample holder, equipped with a knife-edge sharp seal and titanium windows. Experiments were performed in two temperature ranges: (1) ZF-μ^+SR data were collected between 1.4 and 100 K and LF-μ^+SR data at 1.4 K between 10 and 100 Oe using a continuous-flow helium cryostat for a 237-mg sample, and (2) ZF-μ^+SR data were collected between 0.52 and 2 K and LF-μ^+SR data at 0.52 K between 10 and 500 Oe using a ^{3}He sorption cryostat for a 229-mg sample.

In a μ^+SR experiment, 100% spin-polarized positive muons are implanted in the sample. After coming to rest at an interstitial lattice site, they can act as highly sensitive microscopic local magnetic probes, since, under the influence of internal static and dynamic fields, their polarization becomes time dependent. The time evolution of the μ^+ spin polarization, $P_\mu(t)$ ($= A(t)/A_0$, where $A(t)$ is the time dependent asymmetry of the muon histograms, with A_0 the initial asymmetry at $t = 0$) can be monitored by recording time histograms of the muon-decay positrons emitted preferentially along the μ^+ spin direction. In the presence of local internal or external magnetic fields, $<B_\mu>$, the muons undergo Larmor precession with a frequency given by $\nu_\mu = (\gamma_\mu/2\pi)<B_\mu>$, where $\gamma_\mu/2\pi = 13.553\,\mathrm{kHz\,G^{-1}}$ is the muon gyromagnetic ratio. In the absence of an applied external field (ZF), the appearance of a precession in $P_\mu(t)$ signals the onset of an ordering (ferromagnetic or antiferromagnetic) transition. Moreover, application of a magnetic field parallel to the initial μ^+ spin polarization (LF) allows the decoupling of the μ^+ spin from static internal fields.

The ZF-μ^+SR spectra in the high-temperature range of the experiments (Fig. 2f) are characteristic of the presence of weak static nuclear dipole moments, which result in a small depolarization rate, $\sigma \approx 0.06\,\mu\mathrm{s}^{-1}$. These are frozen into a disordered spin configuration, producing a temperature-independent distribution of local fields with a width, $<\Delta B^2>^{1/2} \approx 0.7$ G. An additional very slow relaxation of the μ^+ spin polarization—the spectra were fitted with the product of a Gaussian (σ) and an exponential (λ_d) relaxation, $P_\mu(t) = \exp(-\lambda_d t)\exp(-\frac{1}{2}\sigma^2 t^2)$—is also present ($\lambda_d = 0.012(1)\,\mu\mathrm{s}^{-1}$ at 100 K), arising from extremely rapidly fluctuating electronic moments. Cooling down leads to a small slowing-down of the C_{60}^{3-} spin dynamics within the paramagnetic domains, with the dynamic depolarization rate, λ_d, reaching a value of $0.018(1)\,\mu\mathrm{s}^{-1}$ at 18.2 K.

For temperatures below 18 K, the shape of the ZF-μ^+SR spectra begins to change and becomes more complicated (Fig. 2f). In particular, a rapidly relaxing component starts to become visible at early times and as the temperature is reduced, it gradually begins to dominate. This provides the signature of the onset of freezing of the electronic C_{60}^{3-} moments in excellent agreement with the NMR results. Good fits to the measured data can be obtained in this temperature range by using a two-component relaxation function: $P_\mu(t) = A_1\exp(-\lambda_1 t) + A_2\exp(-\lambda_2 t)$, where A_1 and A_2 are amplitudes reflecting the fractions of the muons contributing to the slowly (paramagnetic) and rapidly (quasi-static) relaxing component, respectively, and λ_1 and λ_2 are their relaxation rates. The physical picture, which is consistent with the evolution of the ZF-μ^+SR spectra in this temperature range, is that of an inhomogeneous form of magnetism with co-existing paramagnetic and spin frozen domains. The relaxation rate of the long-lived component, λ_1, increases gradually on cooling, approaching a value of $0.145(5)\,\mu\mathrm{s}^{-1}$ at 2.5 K that signifies enhanced slowing down of the fluctuating C_{60}^{3-} moments. At the same time, its volume fraction, A_1, decreases to ~0.63 as the short-lived component progressively grows upon cooling the sample to 2.5 K—at this temperature, we can estimate the volume fraction in which muons experience a quasistatic local field as $f_s = 3(1 - A_1)/2 = 0.55$. A further small decrease in temperature to 2.2 K results in a sharp increase in f_s to 0.86, and spin freezing now occurs essentially throughout the whole sample.

Below 2.2 K, the ZF-μ^+SR spectra (Fig. 2f) are dominated by a short-lived component whose shape is very similar to that observed in the fulleride antiferromagnets A15 Cs_3C_{60} and $(NH_3)K_3C_{60}$. While there is no long-lived oscillating component evident even in the high-statistics data at 0.625 K, the asymmetry decays rapidly at time $t < 1.4\,\mu\mathrm{s}$, shows a minimum between 1.4 and 2.0 μs, and recovers at $t > 2.2\,\mu\mathrm{s}$. At longer times, it continues to relax. These characteristics are similar to the features of the dynamic Kubo–Toyabe relaxation function, appropriate for a Gaussian distribution of random fields whose rate decreases with decreasing temperature. Even though this function could provide a reasonable description of the low-temperature magnetic phase, it is inappropriate on the evidence of complementary LF-μ^+SR data collected at 0.52 K in fields up to 100 Oe, which reveal a complete recovery of the asymmetry (Supplementary Fig. 8). As the effect of applied LFs is the decoupling of the depolarization due to dynamic or fluctuating moments from that due to static components, we conclude that the dynamic Kubo–Toyabe description of the ZF-μ^+SR data (which necessitates the presence of fluctuating random fields with rates in excess of $0.6\,\mu\mathrm{s}^{-1}$) is inappropriate, and the origin of the observed relaxation in ZF is quasi-static in nature.

We thus fitted the data at low temperatures with a strongly damped oscillating function superimposed on a slowly relaxing component. The solid line in Fig. 2f is a fit to the 0.625 K data of the function

$$P_\mu(t) = (1/3)\exp(-\lambda_1 t) + (2/3)\exp(-\lambda_2 t)\cos(2\pi\nu_\mu t)$$

where $\nu_\mu = \omega_\mu/2\pi$ is the μ^+ Larmor precession frequency, and λ_1, λ_2 are relaxation rates associated with the two components. The physical origin of the first term in the equation lies with the fact that, on average, for a completely random distribution of the directions of the internal field in a polycrystalline sample, 1/3 of all muons will experience an internal field along their initial spin direction and consequently they will not precess. The relaxation, λ_1, of this 1/3-term is due to fluctuating field components perpendicular to the μ^+ spin and, for the present sample, is of the order of $0.10–0.15\,\mu\mathrm{s}^{-1}$. The damping, λ_2, of the oscillating term in the equation reflects the influence of static field inhomogeneities. At 0.52 K, $\lambda_2 = 1.09(1)\,\mu\mathrm{s}^{-1}$, implying a very broad distribution of the local fields with a width, $<\Delta B^2>^{1/2} = 12.8(1)$ G, comparable to the magnitude of $<B_\mu>$ itself. This evidences the presence of magnetic spatial disorder and inhomogeneity effects. Part of the broadening observed may also arise from the presence of more than one muon stopping site distributed through the structure which will sample the field distribution at different points.